

# Hybrid modelling of a high-power X-ray attenuator plasma

Álvaro Martín Ortega,<sup>a\*</sup> Ana Lacoste<sup>b</sup> and Tiberiu Minea<sup>c</sup>

<sup>a</sup>ESRF – The European Synchrotron, 71 Avenue des Martyrs, 38000 Grenoble, France,

<sup>b</sup>LPSC, Université Grenoble-Alpes, CNRS, IN2P3, 53 Rue des Martyrs, 38026 Grenoble, France, and

<sup>c</sup>Laboratoire de Physique des Gaz et Plasmas-LPGP, UMR 8578 CNRS, Université Paris-Sud,

Université Paris-Saclay, 91405 Orsay Cedex, France. \*Correspondence e-mail: martinor@lpsc.in2p3.fr

Received 7 August 2017

Accepted 14 February 2018

Edited by S. Svensson, Uppsala University, Sweden

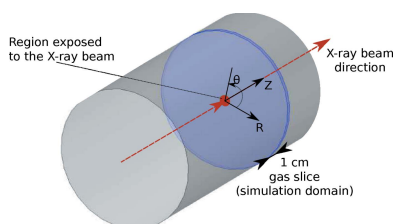
**Keywords:** gas attenuator; X-ray absorption; plasma model; fluid model; Monte Carlo.

X-ray gas attenuators act as stress-free high-pass filters for synchrotron and free-electron laser beamlines to reduce the heat load in downstream optical elements without affecting other properties of the X-ray beam. The absorption of the X-ray beam triggers a cascade of processes that ionize and heat up the gas locally, changing its density and therefore the X-ray absorption. Aiming to understand and predict the behaviour of the gas attenuator in terms of efficiency *versus* gas pressure, a hybrid model has been developed, combining three approaches: an analytical description of the X-ray absorption; Monte Carlo for the electron thermalization; and a fluid treatment for the electron diffusion, recombination and excited-states relaxation. The model was applied to an argon-filled attenuator prototype built and tested at the European Synchrotron Radiation Facility, at a pressure of 200 mbar and assuming stationary conditions. The results of the model showed that the electron population thermalizes within a few nanoseconds after the X-ray pulse arrival and it occurs just around the X-ray beam path, recombining in the bulk of the gas rather than diffusing to the attenuator walls. The gas temperature along the beam path reached 850 K for 770 W of incident power and 182 W m<sup>-1</sup> of absorbed power. Around 70% of the absorbed power is released as visible and UV radiation rather than as heat to the gas. Comparison of the power absorption with the experiment showed an overall agreement both with the plasma radial profile and power absorption trend, the latter within an error smaller than 20%. This model can be used for the design and operation of synchrotron gas attenuators and as a base for a time-dependent model for free-electron laser attenuators.

## 1. Introduction

X-ray gas attenuators are used in high-energy synchrotron beamlines to absorb the low-energy photons from the initial spectrum while letting pass the high-energy ones, thus acting as a high-pass filter. This reduces the heat load on the optical elements, notably the first crystal of double-crystal monochromators (DCMs). If an attenuator is not used, all the power carried by the X-ray beam, of the order of hundreds of W mm<sup>-2</sup> (Biasci *et al.*, 2001) spanning a spectrum of several keV, is absorbed by the DCM. The control of the heat load in the first crystal is essential to avoid thermal deformations on its surface, which otherwise would reduce the transmission at the selected energy and limit the performance of the whole beamline (Chumakov *et al.*, 2004; Zhang *et al.*, 2013).

A gas attenuator is made of a vessel containing a gas, usually argon or krypton, at a pressure which varies depending on the incoming X-ray spectrum and the desired absorption. For example, the gas attenuators at the European Synchrotron



Radiation Facility (ESRF) are between 1 and 2 m long and are operated at pressures between 50 and 500 mbar (Hernández, 2010; Requardt *et al.*, 2013). In contrast, those used at free-electron lasers are usually longer and operate at a lower pressure of a few millibars (Feng *et al.*, 2016; Ryutov *et al.*, 2009).

Previous studies of gas attenuators have focused on the X-ray absorption by the gas, finding that the gas density along the X-ray beam path decreases with respect to the initial one (Hernández, 2010; Requardt *et al.*, 2013). The reason for this is that the power absorbed heats up the gas locally, creating a temperature and a density gradient between the beam path and the walls of the attenuator. A theoretical model developed for the Linear Coherent Light Source-II (LCLS-II) accounts for the gas heating and reproduces the formation of a density gradient (Feng *et al.*, 2016). However, it does not take into account the effect of ionization and excitation of the gas by the X-rays or by the secondary photo- and Auger electrons released after absorption. If the ionization degree is high enough, a plasma will be created within the gas attenuator, changing its properties and triggering a number of processes that may play a fundamental role in the energy transfer. In particular, radiative decay from the excited states may release a significant fraction of the energy as radiation, reducing the amount of heating on the gas. A change of the gas heating will lead to changes in gas temperature and density and therefore in the X-ray absorption.

Plasmas with similar characteristics are those created by high-energy electron beams (Elson & Rokni, 1996; Aleksandrov *et al.*, 2005) and by lithographic extreme-ultraviolet (EUV) lasers (with photon energies of 90 eV and higher) (Beckers *et al.*, 2016). All of these have in common the lack of an applied electric field and a high-energy particle beam as the plasma source. The lack of applied electric fields prevents efficient diffusion of charged particles towards the walls and, if the pressure is high enough (hundreds of mbars), makes volume recombination with diatomic ions the main electron-loss mechanism. At lower pressures (mbar), however, diffusion is still the main electron-loss mechanism.

These plasmas are usually modelled by fluid models in which the transport equations for the particle and energy densities are solved for given boundary conditions (Elson & Rokni, 1996; Aleksandrov *et al.*, 2005). The transport coefficients are calculated assuming a certain electron energy distribution function, or creating a collisional-radiative model for the electron population. However, these models may not be adequate for the modelling of particles in the X-ray energy range (keV), in which they do not behave collectively. Monte Carlo models are typically used to simulate the synchrotron X-rays and nuclear physics processes, for instance in *PENELOPE* (Sempau *et al.*, 1997; Salvat & Fern, 2015) or *Geant4* (Agostinelli *et al.*, 2003; Allison *et al.*, 2006). They are also used to model non-local effects in cold plasmas or in those cases in which the mean free path is comparable with the size of the containing vessel. The plasma in the gas attenuator includes both high- and low-energy processes, so that using only one of the two strategies mentioned above would be

inefficient and computationally demanding; in addition, details of the physical processes involved would be lost. Therefore, to model the gas attenuator processes we have developed a hybrid model that includes analytic, Monte Carlo and fluid sub-models, each of them describing the physics for which they are better adapted.

The paper is organized as follows. In §2 we present the details of the synchrotron radiation properties, in particular those used in the present study. §3 describes the analytic and numerical model, and the results of the model are shown in §4. §5 includes a comparison of the global model with experimental results and a discussion, before presenting the conclusions in the final section.

## 2. Synchrotron radiation properties

Synchrotron radiation is produced when a relativistic electron beam is accelerated perpendicular to its trajectory by a magnetic field, generating a radiation beam in the forward direction with energies of the order of keV. The properties of the X-ray beam generated this way depend on both electron beam energy and magnetic field configuration and strength (Baruchel *et al.*, 1993; Thompson & Vaughan, 2001). The most powerful sources used today are called insertion devices (IDs), in which the electron beam passes through an alternating magnetic field, emitting radiation without changing the net direction. Depending on the amplitude of the electron oscillation, interference phenomena may occur. In the absence of interference, the emitted X-ray beam has a broad, continuous spectrum; these kinds of IDs are called wigglers. If interference occurs, however, the spectrum will consist of a series of peaks, or harmonics, at equally spaced energy intervals; these kind of IDs are called undulators. Both types of IDs are usually capable of changing the strength of the magnetic field and therefore the emitted spectrum properties; this is done by changing the gap between the magnets that create the magnetic field.

Wigglers and undulators are powerful X-ray sources, capable of delivering hundreds of Watts per mm<sup>2</sup> and a total power of several kiloWatts. For instance, the wiggler installed in the biomedical beamline of the ESRF delivers 19.3 kW in a 30 mm × 2 mm aperture (Requardt *et al.*, 2013). The X-ray source used in this study, a U18 in-vacuum undulator, can deliver a power up to 770 W over a 2 mm × 2 mm aperture for the most intense magnetic field (closest gap). The spectrum of this undulator at different gaps is shown in Fig. 1 as calculated by the *Synchrotron Radiation Workshop* (SRW) software (Chubar & Elleaume, 1998). The width of the peaks can be reduced by reducing the beam aperture; the total intensity and power emitted is then also reduced.

The X-ray beams emitted by synchrotron sources are not continuous but have a certain time structure, given by the structure of the electron beam. It is usually characterized by the ‘spread’ in time of the group of electrons, or ‘bunch’, which is usually of a few picoseconds in length. This represents also the time length of each individual X-ray flash. The time between flashes changes depending on the operation mode of

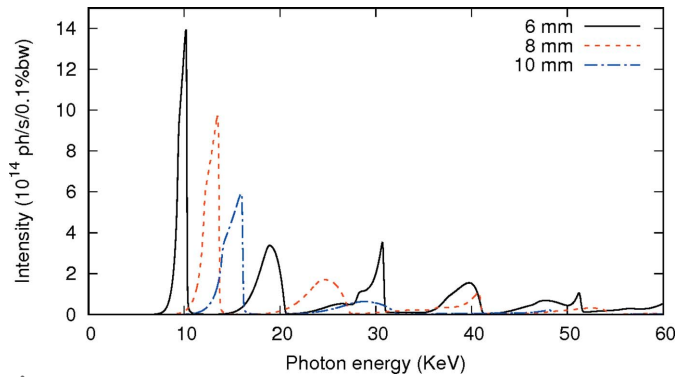


**Figure 1**  
Spectra of the U18 undulator calculated with *SRW* (Chubar & Elleaume, 1998) for 200 mA in the storage ring and  $2\text{ mm} \times 2\text{ mm}$  beam size for several gaps.

each synchrotron. At the ESRF, the most common modes (continuous and 7/8) have 992 bunches equally spaced along the 880 m of circumference, which results in a time between bunches of 2.84 ns, or equivalently a frequency of 352 MHz. Other operation modes are the 16-bunch, with 176 ns of separation between flashes (5.68 MHz), or the 4-bunch, with 704 ns of separation (1.42 MHz). This time structure is relevant because it will determine whether we can treat the X-ray source as continuous, with the plasma reaching a stationary state, or as pulsed, with the plasma showing correspondingly periodic oscillations.

### 3. Numerical model

The numerical model of the gas attenuator is composed of three sub-models, each one describing specific phenomena depending on the energy of the involved species, and based on different approaches: analytic, Monte Carlo and fluid. The relation between the sub-models is represented in the flow chart of Fig. 2. The initial X-ray absorption and the subsequent Auger decay processes are calculated analytically using tabulated cross sections (for the X-ray absorption) and decay probabilities (for the Auger decay). The thermalization of the fast electrons emitted by the previous processes is calculated using a Monte Carlo model, which takes into account the production of secondary electrons, ions and excited species. The output of the Monte Carlo model is used as the plasma source of the fluid model, which calculates the drift, diffusion, recombination, radiative decay and heating of the different particles, including the neutral gas. Because the changes in density calculated by the fluid model will change the X-ray absorption, several iterations between the sub-models are required, in which the radial density profile of the neutral gas obtained in the previous iteration is used to calculate the X-ray absorption in the following one.

To simplify the calculations, the domain of the model will be taken, at this stage, as a two-dimensional (2D) disc of 1 cm depth, with the X-ray beam crossing the centre of the disc perpendicular to its surface (Fig. 3). This simplification is based on the large aspect ratio of most gas attenuators: long cylinders of length 1–2 m and a few millimetres in radius. We

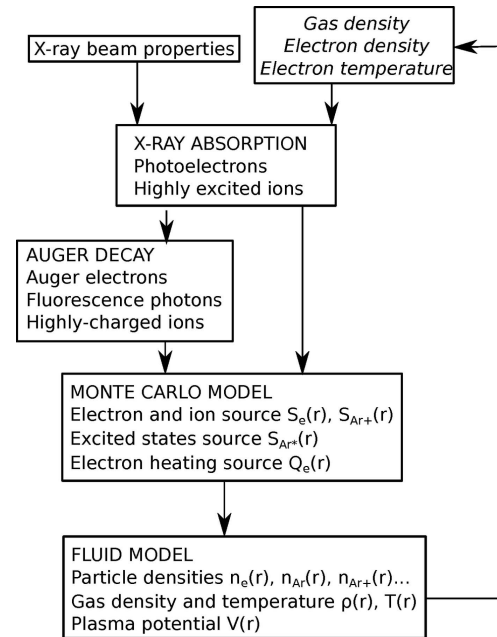


**Figure 2**  
Flow chart of the global model showing the approach used for the gas attenuator numerical model.

expect that the axial gradients will be negligible compared with the radial ones, and therefore we can ignore the axial coordinate in a first approximation. The time structure of the X-ray beam will be taken into account in the high-energy part of the model, simulating the absorption of a single X-ray flash and the temporal evolution of the produced electrons. This time information is averaged in the fluid model, in which a continuous source is assumed.

#### 3.1. X-ray photon absorption

The absorption of the X-ray beam is described by the Beer–Lambert law,

$$\frac{dI(E)}{dz} = -I(E)\sigma(E)\rho(z), \quad (1)$$

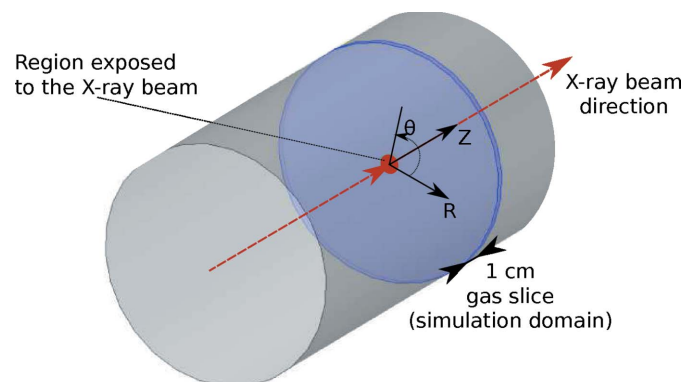


**Figure 3**  
Scheme of the simulation domain, consisting on a 2D disc perpendicular to the beam path. The longitudinal position of the disc can be adjusted in the model. The region of the X-ray beam is marked in red.

where  $I$  is the beam intensity at each energy,  $\sigma$  is the total cross section and  $\rho$  is the gas density. In the X-ray energy range the dominant process is photoionization, while at higher energies Compton scattering dominates, but with a rather small cross section so that the gas becomes virtually transparent (Cullen *et al.*, 1997; Saloman *et al.*, 1988). The resulting particles from the photoionization are the released photoelectrons and the ions with a vacancy in an inner shell. The number of photoelectrons can be calculated analytically,

$$N_{e,X}(E - E_X) = N_\gamma(E) \frac{\sigma_X(E)}{\sigma_T(E)} \left\{ 1 - \exp[\rho \sigma_T(E) \Delta z] \right\}, \quad (2)$$

where  $N_{e,X}$  is the number of photoelectrons emitted from the  $X$  shell ( $X = K, L_1, L_2, L_3, \dots$ ),  $E_X$  and  $\sigma_X$  are the binding energy and cross section of the  $X$  shell, respectively,  $\sigma_T$  is the total cross section of the photon processes and  $N_\gamma$  is the number of incoming photons. The initial energy of the photoelectrons is that of the absorbed X-ray photon minus the binding energy of the atomic shell. The integral over the energy of the photons emitted from the  $X$  shell provides the total number of ions produced with a vacancy in the mentioned shell. These ions are in a highly excited state and will decay *via* Auger and fluorescence mechanisms, which will produce further high-energy electrons and also a highly charged ion population, as detailed in §3.2.

The model calculates the amount of X-ray absorption as well as the number of electrons and ions produced, assuming a constant gas mass density in the X-ray beam area. Due to their larger mass, the ions are assumed to remain stationary during the thermalization of the electrons, *i.e.* they will not be considered in the Monte Carlo model. The photoelectrons, on the other hand, are emitted with a large kinetic energy, following an angular distribution given by the Sauter–Gavrila differential cross section (Gavrila, 1959), and their trajectories need to be simulated in detail. Although the relatively high gas pressure and neutral atom density will make the velocity distribution rapidly become isotropic, by keeping the angular distributions we expect our model to be valid also in cases with a lower gas pressure and particle density.

### 3.2. Auger decay

The number of multiply charged ions, fluorescent photons and Auger electrons emitted from inner-shell ions is calculated analytically, using the emission probabilities of the complete cascade. If the probability of having an electron of energy  $E_i$  emitted from an ion with a vacancy in the  $X$  shell ( $X = K, L, M, \dots$ ) is represented as  $P_e(E_i, X)$  and the total number of ions with an  $X$  vacancy is  $N_{Ar,X}$  (obtained from the photon absorption calculation), then the number of emitted electrons  $N_e$  is calculated as

$$N_e(E_i) = P_e(E_i, X) N_{Ar,X}. \quad (3)$$

As each ion will emit several particles (electrons and photons) during the cascade, the sum of probabilities might be higher than 1:  $\sum_i P(E_i, X) \neq 1$ . A similar formula is used to calculate the final charge state of the ions after the cascade:

$$N_{Ar}(n+) = P_{Ar}(n+, X) N_{Ar,X}, \quad (4)$$

where  $P_{Ar}(n+, X)$  is the probability of an ion of initial vacancy in  $X$  to end up with a total charge of  $n+$ , and  $N_{Ar}(n+)$  is the total number of ions with that charge after the cascade. In this case the sum of probabilities must be 1 because each ion only increases its charge:  $\sum_n P_{Ar}(n+, X) = 1$ .

The final charge state probabilities are reported in the literature (Carlson *et al.*, 1966; Abdullah *et al.*, 2003); however, the Auger and fluorescence emission probabilities available at the Evaluated Atomic Data Library (EADL) (Perkins *et al.*, 1991b) include only the first decay of the cascade from the inner-shell ions. We use the data on the EADL to build a separate model (Monte Carlo) of the complete cascade similar to the one made by Abdullah *et al.* (2003) and assuming that the decay ratios are only modified proportionally to the number of electrons in the upper shells. This way, the fluorescence emission probability following a transition from shells  $X$  (upper) to  $Y$  (lower) ( $X, Y = K, L_1, L_2, L_3, \dots$ ) is reduced by a factor  $(E - V)/E$ , where  $E$  is the total number of electrons in the  $X$  shell and  $V$  is the number of vacancies. In the case of Auger emission, the probability is modified by the same factor as well as a similar one from the shell emitting the Auger electron. We are introducing some error by not modifying the probabilities further; however, we expect that the current model will be accurate enough to capture the effect of the cascade and account for the extra charges produced in the process. Note that this calculation is not part of the gas attenuator model: once the probabilities of the cascade for a given gas are known, they can be re-used for any simulation using the same gas.

For each initial inner shell vacancy, a large number of cascades ( $10^8$ ) were simulated as in Abdullah *et al.* (2003). The first decay of the cascade is sampled randomly among all the possible different decays, whose sum equals 1. The released particle type (photon or electron), its energy and the new state of the ion is recorded. If the ion still has vacancies on its inner shells, the process is repeated, modifying the probabilities to take into account any additional vacancy in an upper shell. The cascade stops when all the vacancies are in the outer shells. Once the probabilities of the complete cascades are known, they are multiplied by the total number of inner shell ions following equations (3) and (4) to obtain the total number and energy of Auger electrons and the total number of relaxed, multiply charged ions. An instance of the results of these calculations is shown in Figs. 4 and 5 for Auger electrons and multiply charged ions, respectively, for the following operating conditions: 200 mbar of argon, X-ray beam of 2 mm  $\times$  2 mm and a spectrum corresponding to a 6 mm gap in a U18 undulator. The decay occurs in the region exposed to the X-ray beam, where the absorption occurs. These results are the output of the analytic model. The results of the Auger electron population are further used as input for the next model block, Monte Carlo. The transport of the resulting fluorescent photons is not simulated; rather, it is assumed that they reach the walls of the attenuator without further interaction with the gas. The estimation of their effect

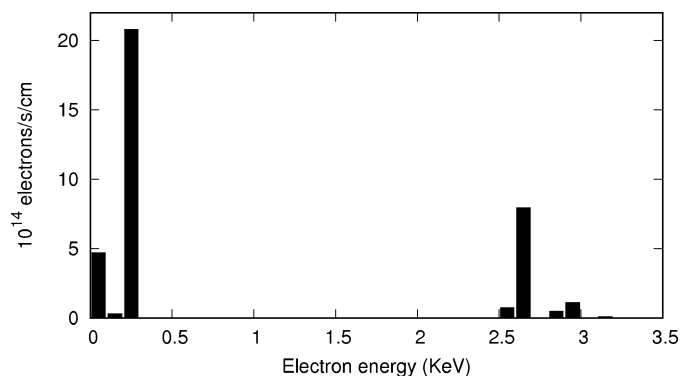


**Figure 4** Histogram of the Auger electron population after relaxation of the inner-shell argon ions, assuming an X-ray beam of  $2\text{ mm} \times 2\text{ mm}$ , and an incident spectrum corresponding to a U18 undulator at 6 mm gap (Fig. 1). Bin size: 100 eV.

was found to be negligible for the charge production (not shown).

### 3.3. Monte Carlo model of the electron thermalization

**3.3.1. Cross sections.** The objective of the Monte Carlo (MC) model is to simulate the thermalization of the energetic electrons and the cascade of processes they trigger from their initial energy down to a few eV. Due to the large energy range of the slow-down process (from keV to a few eV), the cross sections have been taken from two databases, the Evaluated Electron Data Library (EEDL; Perkins *et al.*, 1991a) and the LXCat (Bordage *et al.*, 2013). The EEDL is a reference database for nuclear physics, used in *PENELOPE* (Sempau *et al.*, 1997; Salvat & Fern, 2015) and in *Geant4* (Agostinelli *et al.*, 2003; Allison *et al.*, 2006), and accurate from a few hundreds of eV to the GeV range. It includes electron ionization collisions for each subshell but only a single inelastic cross section. LXCat, on the other hand, is a compilation of databases built for low-temperature plasma research, to calculate reaction rates and transport coefficients in the eV range among other objectives. The data used here were that of the *MagBolz* program (Biagi, 2015), similar to the values found in other

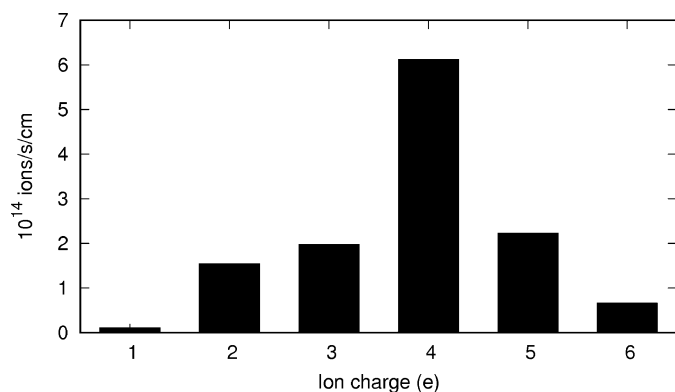


**Figure 5** Histogram of the multiply charged argon ions after relaxation of the inner-shell argon ions, assuming an X-ray beam of  $2\text{ mm} \times 2\text{ mm}$ , and an incident spectrum corresponding to a U18 undulator at 6 mm gap (Fig. 1).

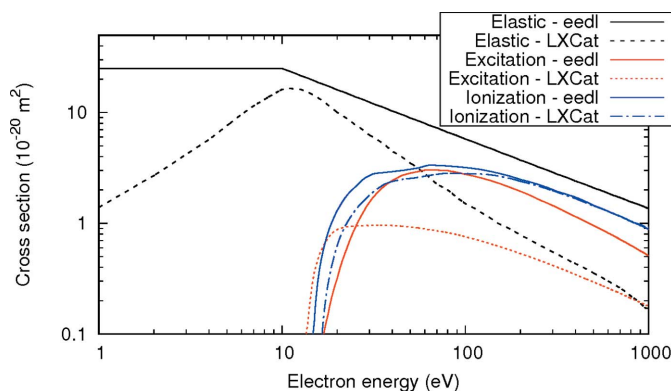


**Figure 6** Comparison of the electron impact cross section collected from two databases, LXCat (Bordage *et al.*, 2013) and EEDL (Perkins *et al.*, 1991a), for elastic, inelastic and ionization collisions. The different scope of each database (eV range for LXCat, keV and higher for EEDL) results in different results for the cross sections.

databases included in LXCat. It includes the excitation cross section for every excited level but only a single ionization cross section from the outermost shell, the only one possible for the low-energy electrons. The problem is that, due to their different scope, the two databases give different cross sections in the overlapping region (Fig. 6). The solution taken here is to use the high-energy EEDL database for electron energy above 100 eV and LXCat for the rest. The effect of the discontinuity in the cross sections was studied by shifting the mentioned 100 eV threshold to 1 keV; the impact in the final results was negligible.

The high-energy electrons also carry enough energy to ionize multiple times an atom in a single interaction process. While these collisions (direct multiple ionization) are less likely than the single ionization collisions, the multiple charged ions may play a role due to their higher sensitivity to electric fields and to their higher internal energy with respect to single-charged ions. The cross sections used here have been taken from Kobayashi *et al.* (2002).

In addition to the electron–neutral collisions, electron–electron (Coulomb) collisions (Takizuka & Abe, 1977; Hussein *et al.*, 1992) have been included in the model. Once the first loop of the hybrid model is achieved, the electrons simulated in the MC model may undergo Coulomb collisions with the background electron population calculated by the low-energy fluid model in the previous loop. Note that we are assuming that the background electron population is not disturbed with the arrival of the electrons of the following pulse. The collisions between two fast electrons, *i.e.* between two electrons simulated in the MC model, is neglected for now, assuming that its number density is small compared with the background population. This assumption will be verified *a posteriori*, comparing the respective electron densities in §4.2.

**3.3.2. Energy loss and scattering angle.** The scattering angle of the electrons after a collision with an atom is sampled from the following distribution (Verboncoeur, 2005; Vahedi & Surendra, 1995),

$$\cos(\theta) = \left[ \frac{2 + E - 2(1 - E)^R}{E} \right], \quad (5)$$

where  $E$  is in eV and  $R$  is a random number between 0 and 1. This distribution arises from the known elastic differential cross section. The polar angle  $\varphi$  is sampled randomly between 0 and  $2\pi$ . The energy of the scattered electron depends on the collision type. For elastic collisions it can be obtained from classical energy and momentum conservation laws,

$$E_e = E_{e_0} \left\{ 1 - \frac{2m_e}{M} [1 - \cos(\theta)] \right\}, \quad (6)$$

where  $E_{e_0}$  is the initial energy,  $E_e$  the final energy, and  $M$  and  $m_e$  the atom and electron mass, respectively. For excitation collisions, the energy loss is determined by

$$E_e = E_{e_0} - E_{\text{exc}}, \quad (7)$$

where  $E_{\text{exc}}$  is the threshold energy. For ionization collisions, the energy loss is calculated as

$$E_e = E_{e_0} - E_{\text{ion}} - \sum_n E_{n,\text{sec}}, \quad (8)$$

where  $E_{\text{ion}}$  is the ionization energy and  $E_{n,\text{sec}}$  is the kinetic energy of the secondary electrons released. The latter is calculated from the following distribution,

$$P(E_{\text{sec}}) = B \tan\left(\frac{E_0 - E_{\text{ion}}}{B}\right), \quad (9)$$

where  $B$  is an element-dependent parameter whose value for argon is 10 (Opal *et al.*, 1971). From this distribution one can calculate the cumulative distribution function and invert it to obtain the secondary electron energy from a random sampling. The emission angle of the secondary electron is taken as random.

**3.3.3. Algorithm.** The MC model is made time-dependent, so that it is possible to study the particle populations at any time after the initial time. The time  $t = 0$  is chosen as the instant when an individual X-ray pulse crosses the attenuator and the photoionization and Auger decay takes place. The few picoseconds of delay in the Auger decay is neglected here. The trajectory of these electrons is then simulated in three dimensions (3D), and the number of secondary particles created recorded. Because we do not consider interactions between electrons generated at the same pulse, each electron is simulated individually before starting with the following one.

The collisions are treated using the null collision technique initially proposed by Skullerud (1968) and improved by Brennan (1991). It considers a collision frequency constant and is equal to the maximum value:  $f = \max(N\sigma v)$ , where  $\sigma$  is the sum of the cross sections,  $v$  the electron velocity and  $N$  the heavy particle density. This is equivalent to adding an additional collision process so that the total cross section remains constant. The flight time  $\tau$  between collisions is then calculated as

$$\tau = -\log(1 - P)/f, \quad (10)$$

where  $P$  is a random number between 0 and 1. The kind of collision is obtained from a second random number sampling, using the cumulative sum of the cross sections or, equivalently, the partial collision frequencies. If the collision corresponds to the null collision, the energy and direction of the particle remains unchanged. If it is one of the ‘true’ collisions, the energy and direction are modified as explained in the previous section.

When an ionization collision takes place, the position, energy and direction of the secondary electron is saved and simulated later. The criteria to finish the simulation is a time set manually by the user. It should be set so that at the end of the simulation most of the electrons have an energy less than the smallest excitation energy. Prolonging the simulation further will result only in the diffusion of the cold electrons towards the attenuator walls, since no electric field will accelerate them again to higher energies. These phenomena are the core of the fluid simulation and they are treated in the specific part of the hybrid model, described in the following section. Once the simulation is completed, the resulting 3D population is projected over the radial coordinate of a cylindrical coordinate system, and the resulting spatial and energy distributions sent as input for the fluid model.

### 3.4. Fluid model

The objective of the fluid model is to calculate the steady state of the plasma inside the gas attenuator, by taking as input the particle source of the MC model and calculating the solution to the transport equations for all considered plasma species, the Poisson equation for the electric field and the heat transfer for the gas temperature and density. For this purpose we have used the commercial finite-element analysis software *COMSOL Multiphysics*<sup>®</sup> (COMSOL, 2017a,b). The main output of the fluid model is the gas temperature and density profiles as a function of the attenuator radius: its value at the attenuator axis is used by the high-energy model to calculate the X-ray absorption in the next iteration. The electric field (self-consistently produced by the plasma itself) and electron density are also used to calculate the effect of electric forces and Coulomb collisions, respectively. Other outputs like the power balance, plasma potential, electron temperature or particle concentration profile will be used to better understand the physics of the attenuator.

**3.4.1. Plasma species.** The chemical species considered in the fluid model for argon gas are electrons, neutral atoms Ar, first and second excited levels blocks  $\text{Ar}^s$  and  $\text{Ar}^p$  (each of them treated as a single effective level), single and double charged monoatomic ions  $\text{Ar}^+$  and  $\text{Ar}^{++}$ , diatomic and triatomic ions  $\text{Ar}_2^+$  and  $\text{Ar}_3^+$  and one excimer state  $\text{Ar}_2^*$ . A similar model was developed for krypton, without considering the triatomic ions which were found to play a negligible role in the argon simulations. The present work details only the model for argon.

**3.4.2. Governing equations.** The time-dependent electron continuity equation solved for this problem can be written as

$$\frac{\partial n_e}{\partial t} + \nabla \cdot \Gamma_e = R_e, \quad (11)$$

$$\Gamma_e = -\mu_e \mathbf{E} n_e - D_e \nabla n_e,$$

where  $n_e$  is the electron density,  $\Gamma_e$  is the electron particle flux and  $R_e$  is the net source term, *i.e.* the production and loss terms of the electrons, which includes both the input from the MC model and the gains and losses due to ionization and recombination, respectively. The electron particle flux  $\Gamma_e$  is given by the drift-diffusion relation that contains the kinetic parameters, namely the mobility of the electrons in the presence of the electric field  $\mathbf{E}$ , denoted  $\mu_e$ , and the diffusion of the electrons due to their density gradient, denoted  $D_e$ . Because of the absence of applied magnetic fields, the transport coefficients are scalar quantities. An equivalent equation is written for the electron energy conservation,

$$\frac{\partial n_\varepsilon}{\partial t} + \nabla \cdot \Gamma_\varepsilon + \mathbf{E} \cdot \Gamma_e = Q_\varepsilon, \quad (12)$$

$$\Gamma_\varepsilon = -\mu_\varepsilon \mathbf{E} n_\varepsilon - D_\varepsilon \nabla n_\varepsilon,$$

where  $n_\varepsilon$  is the electron energy density,  $\Gamma_\varepsilon$  is the electron energy flux and  $Q_\varepsilon$  is the energy gain and loss by the electron population, including the input from the MC module (in this case the kinetic energy associated with the electron population) and the energy exchanged in ionization, recombination, elastic and inelastic collisions. The additional term  $\mathbf{E} \cdot \Gamma_e$  on the left-hand side of the equation accounts for the Joule heating (or Ohmic heating) of the electron population in the presence of the electric field. The electron energy flux  $\Gamma_\varepsilon$  is determined by the energy mobility coefficient  $\mu_\varepsilon$  and energy diffusion coefficient  $D_\varepsilon$ . The mean electron energy is obtained from the solution of the two equations described above, as the ratio between the electron particle density and the electron energy density,  $\bar{\varepsilon} = n_\varepsilon/n_e$ . Assuming a Maxwellian electron energy distribution function (EEDF), the electron temperature can be calculated (in energy units) as  $T_e = (2/3)\bar{\varepsilon}$ .

An identical continuity equation can be written for the transport of the heavy species (ions and neutral atoms) of the plasma,

$$\frac{\partial n_X}{\partial t} + \nabla \cdot \Gamma_X = R_X, \quad (13)$$

$$\Gamma_X = -\mu_X \mathbf{E} n_X - D_X \nabla n_X.$$

This is equivalent to the electron continuity equation (11) where  $X$  stands for every heavy species of the model. The electric field only affects the charged particles, while the neutral species are only affected by the diffusion. The reduced mobilities of the different ion species were taken as  $3.75 \times 10^{19} \text{ V}^{-1} \text{ m}^{-1} \text{ s}^{-1}$  for  $\text{Ar}^+$  (Petrov & Ferreira, 2013),  $7.0617 \times 10^{19}$  for  $\text{Ar}^{++}$  (Bogaerts & Gijbels, 1999) and  $4.4871 \times 10^{19}$  for  $\text{Ar}_2^+$  and  $\text{Ar}_3^+$  (Petrov & Ferreira, 2013). The diffusion coefficient of the ions was calculated from the mobility using the Einstein relation,  $D = \mu k_B T/q$ , where  $k_B$  is the Boltzmann constant,  $q$  the ion charge and  $T$  the gas temperature. The reduced diffusion coefficient of the neutral species was taken

as a constant value equal to  $3.54 \times 10^{18} \text{ m}^{-1} \text{ s}^{-1}$  (Bogaerts & Gijbels, 1999). The total number of heavy species particles and the gas mass density are related to each other, so that if the gas pressure is one of the input parameters, as it is in our case, one of the continuity equations must be dropped and replaced by the ideal gas law. This way the total number of heavy species particles in the system is adjusted to obtain the imposed gas pressure. In our case we replaced the neutral gas transport equation by the ideal gas law,

$$p = nRT, \quad (14)$$

where  $R$  is the ideal gas constant,  $n$  the number density and  $p$  the gas pressure. Only one equation is written for the heat transfer of all the heavy species considered (ions and excited states), assuming that because of their similar masses the energy exchange between them is efficient and leads to a single energy distribution. This distribution is characterized by a gas temperature  $T$  calculated from the heat equation,

$$\rho C_p \frac{\partial T}{\partial t} - \nabla(k\nabla T) = Q_{\text{gas}}, \quad (15)$$

where  $C_p$  is the heat capacity at constant pressure,  $k$  is the thermal conductivity and  $Q_{\text{gas}}$  is the heat source term, including heating by elastic collisions with electrons, and heating and cooling by chemical reactions. The heat conductivity and heat capacity were chosen as those of argon gas (Bich *et al.*, 1990), as it was assumed that the effect of other heavy species in the heat transport would be negligible.

The electric field  $\mathbf{E} = -\nabla V$  is obtained *via* the electric potential  $V$ , which is in turn calculated solving the Poisson equation

$$\nabla^2 V = \frac{\rho_q}{\varepsilon_0}, \quad (16)$$

where  $\varepsilon_0$  is the vacuum permittivity constant and  $\rho_q$  is the net charge density. Note that because of the absence of an applied voltage the resulting electric field will correspond to the ambipolar electric field, except near the attenuator wall where a sheath develops.

*Boundary conditions.* The simulation domain is a 2D azimuthally symmetric slice of the attenuator; the gradients and fluxes written above are in this case a function only of the radial position. The boundary conditions at the centre of the domain are the same for all the equations and dictated by the symmetry of the problem: the derivative of every variable must be zero,

$$\left. \frac{\partial X}{\partial r} \right|_{r=0} = 0, \quad (17)$$

where  $X$  is the variable considered. The boundary conditions at the wall of the attenuator correspond to those of an absorbent material, *i.e.* any electron, ion and excited species reaching the wall will be absorbed by it. Their energy is accounted for as transmitted to the wall and in the case of heavy particles (ion, excited states) they are re-injected in the gas phase as neutral ground-state atoms. The absence of an applied electric field means that the only field facing the

**Table 1**  
List of reactions included in the argon fluid model.

#	Reaction	Reaction coefficient	Reference
Electron-impact reactions (cross sections)			
1	$e + \text{Ar} \rightarrow e + \text{Ar}$		
2	$e + \text{Ar} \rightarrow e + \text{Ar}^s$		
3	$e + \text{Ar} \rightarrow e + \text{Ar}^p$		
4	$e + \text{Ar}^s \rightarrow e + \text{Ar}$		
5	$e + \text{Ar}^p \rightarrow e + \text{Ar}$		
6	$e + \text{Ar} \rightarrow 2e + \text{Ar}^+$	LXCat and <i>BOLSIG+</i>	Biagi (2015), Hagelaar & Pitchford (2005)
7	$e + \text{Ar}^s \rightarrow 2e + \text{Ar}^+$		
8	$e + \text{Ar}^p \rightarrow 2e + \text{Ar}^+$		
9	$e + \text{Ar}^s \rightarrow e + \text{Ar}^p$		
10	$e + \text{Ar}^p \rightarrow e + \text{Ar}^s$		
11	$e + \text{Ar}_2^s \rightarrow 2e + \text{Ar}_2^+$	Cross section and <i>BOLSIG+</i>	Vriens & Smeets (1980), Petrov & Ferreira (2013)
Recombination reactions			
12	$e + \text{Ar}_2^+ \rightarrow \text{Ar} + \text{Ar}^p$	$8.5 \times 10^{-7} (T_e[\text{K}]/300)^{-0.67} (T[\text{K}]/300)^{-0.58} \text{cm}^3 \text{s}^{-1}$	Mehr & Biondi (1968)
13	$2e + \text{Ar}_2^+ \rightarrow e + \text{Ar} + \text{Ar}^p$	$5.4 \times 10^{-27} T_e[\text{eV}]^{-4.5} \text{cm}^6 \text{s}^{-1}$	Biberman <i>et al.</i> (1987)
14	$e + \text{Ar} + \text{Ar}_2^+ \rightarrow 2\text{Ar} + \text{Ar}^p$	$3.7 \times 10^{-29} T_e[\text{eV}]^{-1.5} T[\text{K}]^{-1} \text{cm}^6 \text{s}^{-1}$	Biberman <i>et al.</i> (1987)
15	$2e + \text{Ar}^+ \rightarrow e + \text{Ar}^p$	$5.4 \times 10^{-27} T_e[\text{eV}]^{-4.5} \text{cm}^6 \text{s}^{-1}$	Biberman <i>et al.</i> (1987)
16	$e + \text{Ar} + \text{Ar}^+ \rightarrow \text{Ar} + \text{Ar}^p$	$3.7 \times 10^{-29} T_e[\text{eV}]^{-1.5} T[\text{K}]^{-1} \text{cm}^6 \text{s}^{-1}$	Biberman <i>et al.</i> (1987)
17	$e + \text{Ar}_3^+ \rightarrow 2\text{Ar} + \text{Ar}^p$	$1.6 \times 10^{-7} T_e[\text{eV}]^{-0.54} \text{cm}^3 \text{s}^{-1}$	Elson & Rokni (1996)
18	$2e + \text{Ar}_3^+ \rightarrow e + \text{Ar} + \text{Ar}_2^s$	$5.4 \times 10^{-27} T_e[\text{eV}]^{-4.5} \text{cm}^6 \text{s}^{-1}$	Biberman <i>et al.</i> (1987)
19	$e + \text{Ar} + \text{Ar}_3^+ \rightarrow 2\text{Ar} + \text{Ar}_2^s$	$3.7 \times 10^{-27} T_e[\text{eV}]^{-1.5} T[\text{K}]^{-1} \text{cm}^6 \text{s}^{-1}$	Biberman <i>et al.</i> (1987)
Heavy species reactions			
20	$2\text{Ar}^s \rightarrow e + \text{Ar} + \text{Ar}^+$	$5 \times 10^{-10} \text{cm}^3 \text{s}^{-1}$	Elson & Rokni (1996)
21	$\text{Ar}^s + \text{Ar}^p \rightarrow e + \text{Ar} + \text{Ar}^+$	$5 \times 10^{-10} \text{cm}^3 \text{s}^{-1}$	Elson & Rokni (1996)
22	$2\text{Ar}^p \rightarrow e + \text{Ar} + \text{Ar}^+$	$5 \times 10^{-10} \text{cm}^3 \text{s}^{-1}$	Elson & Rokni (1996)
23	$2\text{Ar}^s \rightarrow e + \text{Ar}_2^+$	$5 \times 10^{-10} \text{cm}^3 \text{s}^{-1}$	Elson & Rokni (1996)
24	$2\text{Ar} + \text{Ar}^+ \rightarrow \text{Ar} + \text{Ar}_2^+$	$9.4 \times 10^{-33} T[\text{K}]^{-0.27} \text{cm}^6 \text{s}^{-1}$	Chen (1969)
25	$\text{Ar}^s + \text{Ar} \rightarrow 2\text{Ar}$	$3 \times 10^{-21} \text{cm}^3 \text{s}^{-1}$	
26	$\text{Ar}^p + \text{Ar} \rightarrow \text{Ar}^s + \text{Ar}$	$5 \times 10^{-11} \text{cm}^3 \text{s}^{-1}$	Chang & Setser (1978)
27	$\text{Ar}^p + 2\text{Ar} \rightarrow \text{Ar}^s + 2\text{Ar}$	$5 \times 10^{-32} \text{cm}^6 \text{s}^{-1}$	Chang & Setser (1978)
28	$\text{Ar}^s + 2\text{Ar} \rightarrow \text{Ar}_2^s + \text{Ar}$	$10^{-32} \text{cm}^6 \text{s}^{-1}$	Oka <i>et al.</i> (1979)
29	$2\text{Ar} + \text{Ar}_2^+ \rightarrow \text{Ar} + \text{Ar}_3^+$	$6.96 \times 10^{-32} (T[\text{K}]/298)^{-0.47} \text{cm}^6 \text{s}^{-1}$	Turner & Conway (1979)
30	$\text{Ar} + \text{Ar}_3^+ \rightarrow 2\text{Ar} + \text{Ar}_2^+$	$8.65 \times 10^{-12} (T[\text{K}]/298)^{-0.73} \text{cm}^3 \text{s}^{-1}$	Turner & Conway (1979)
31	$\text{Ar} + \text{Ar}^{+2} \rightarrow 2\text{Ar}^+$	$4.1 \times 10^{-13} \text{cm}^3 \text{s}^{-1}$	Howorka (1977)
Radiative decays			
32	$\text{Ar}^s \rightarrow \text{Ar} + h\nu$	$6.25 \times 10^6 \text{s}^{-1}$	Wiese & Martin (1980)
33	$\text{Ar}^p \rightarrow \text{Ar}^s + h\nu$	$3.76 \times 10^8 \text{s}^{-1}$	Wiese & Martin (1980)
34	$\text{Ar}_2^s \rightarrow 2\text{Ar} + h\nu$	$3.5 \times 10^5 \text{s}^{-1}$	Neeser <i>et al.</i> (1997)

attenuator wall is the sheath field; we assume that it is small so that secondary electron emission induced by the ions striking the wall is negligible. This assumption is verified *a posteriori* in §4.2. The boundary condition at the wall can be written as

$$X(r = R) = 0. \quad (18)$$

The only exception concerns the gas temperature at the wall. Indeed, as the wall is water-cooled and kept at a constant temperature of 300 K, the neutral gas atoms are assumed to be in thermal equilibrium with the wall. Therefore, according to the ideal gas law, the density of neutral ground-state atoms remains at a value given by  $n_{\text{wall}} = p/RT_{\text{wall}}$ .

**3.4.3. Reactions.** The reactions included in the argon gas model are shown in Table 1. They include electron collision cross sections, recombination of electrons *via* three-body processes and with diatomic and triatomic ions, conversion from atomic to molecular ions, excimer production and radiative deexcitation of excited species.

The reaction rates of the electron-impact reactions were calculated as a function of the mean electron energy by using the program *BOLSIG+* (Hagelaar & Pitchford, 2005) and

cross sections obtained from the Biagi database on LXCat (Biagi, 2015), assuming a Maxwellian EEDF for the transport coefficients. The recombination reactions are not usually given with a cross section but rather as a reaction coefficient, a function of gas and electron temperature (Mehr & Biondi, 1968; Biberman *et al.*, 1987). This temperature-dependent coefficient is also found for heavy species reactions like the molecular ion formation (Chen, 1969). Coefficients with gas and electron temperature dependence have been used when available to account for the thermal gradients expected in the gas.

The radiative deexcitations coefficients are of extreme importance because the power emitted in this way will reach the attenuator walls without heating either the electrons or the gas. The lifetime of the  $\text{Ar}^p$  effective level has been taken directly from the literature (Wiese & Martin, 1980), as well as for the  $\text{Ar}_2^s$  excimer state (Neeser *et al.*, 1997). However, for the  $\text{Ar}^s$  states the mixture between resonant and metastable states at high pressure requires taking into account the exchange between levels due to electron collisions (Carbone *et al.*, 2013) and the radiation trapping of the emitted UV

photons (Mills & Hieftje, 1984). These effects can be approximated by a longer effective lifetime of the  $\text{Ar}^s$  level block, which in our case is of the order of microseconds.

The largest possible number of reactions was included in the model to make it as general as possible. Many reactions will play only a secondary role in the particle and energy densities and could be removed from the simulation without effecting the final result. However, this balance is only verifiable *a posteriori* and valid only for a specific set of input parameters, like range of gas pressure or of power absorption. By including a rich kinetics we expect to be able to use the same model for a wider range of working conditions.

#### 4. Modelling results

The described model was used to simulate the X-ray absorption by a gas attenuator of 18 mm radius, 55 cm length and 200 mbar of pressure. The incoming X-ray beam had the characteristics of the U18 undulator with 6 mm gap (Fig. 1) and  $2\text{ mm} \times 2\text{ mm}$  size, and the total power carried by the beam was of 770 W. The simulation parameters were chosen equal to those used in an experimental study of a gas attenuator (Martín Ortega *et al.*, 2017). The 2D simulation was performed at several  $Z$  positions along the attenuator; the results shown in this section correspond to the position of  $z = 0$ , with the incoming X-ray beam not attenuated by any previous volume of gas. First we will show the output of the MC model, to study the temporal evolution of the electron population generated after the arrival of an X-ray flash, to verify whether we can treat the plasma source in the fluid model as continuous or pulsed. The results of the fluid model will be shown later, including the final gas temperature and density and a power balance between the different processes involved. The results of both MC and fluid models are taken from the last iteration of the simulation loop, when convergence is already achieved.

##### 4.1. Electron thermalization

The evolution of the electron energy distribution function is shown in Fig. 7 for several time delays after the arrival of the simulated X-ray pulse. The photoionization and Auger decay are assumed to occur instantaneously and simultaneously. One can observe that the electron population grows significantly during the first 0.5 ns; after that time the number of electrons at energies below 2 eV keeps growing, while the population at higher energies decreases. The depletion of the electron population is especially relevant for energies above 11 eV, corresponding roughly to the lowest excitation energy of the first excited state (effective block  $\text{Ar}^s$ ). This means that after around 5 ns (for this particular pressure of 200 mbar) virtually all the electron-heavy species collisions become elastic, and only a redistribution of the energy will occur. This is also the reason for not continuing the MC simulation any further: the diffusion and thermalization of electrons at this pressure will take too long to simulate with this technique, while it can be efficiently simulated by a fluid model without losing any

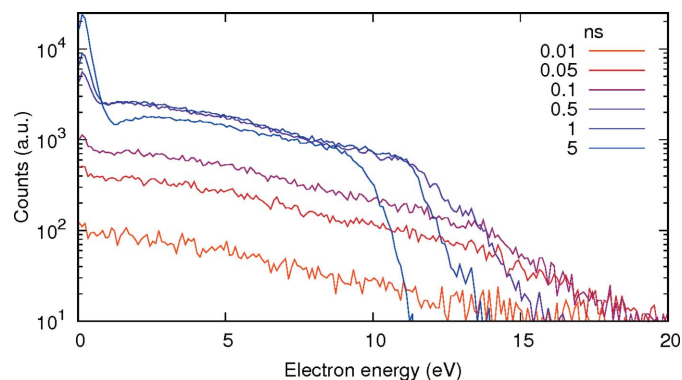


**Figure 7**  
Histogram of the simulated electron population energy distribution at different simulation times after the arrival of an X-ray flash. The plot only shows the low-energy electrons ( $<20\text{ eV}$ ). Simulation for 200 mbar Ar,  $2\text{ mm} \times 2\text{ mm}$  beam size, U18 undulator spectrum (see Fig. 1). Bin size: 0.1 eV.

information or the effects of fast electrons that we see have already disappeared. Also, the fluid model simulates the losses of electrons in the bulk of the plasma by electron-ion recombination, which happens only at low electron energy, and this has not been included in the MC model.

The increase of the electron population during the first nanosecond can also be seen in the spatial distribution of the electrons (Fig. 8). The density increases sharply in the area exposed to the X-ray beam (grey region in Fig. 8), while diffusing only slowly towards the attenuator walls. After the first nanosecond the increase stops and only diffusion governs the electron distribution; 5 ns after the X-ray absorption the density in the central region has started to decrease (the maximum electron density at 1 ns is higher than at 5 ns). This tendency can be clearly seen by comparing the total number of electrons in the simulation (Fig. 9): the number of electrons stays almost constant after 1 ns, illustrating a saturation of the number of new electrons produced by ionization cascades, in line with their low energy. In subsequent simulations, the simulation time will be chosen so that at the end of this time

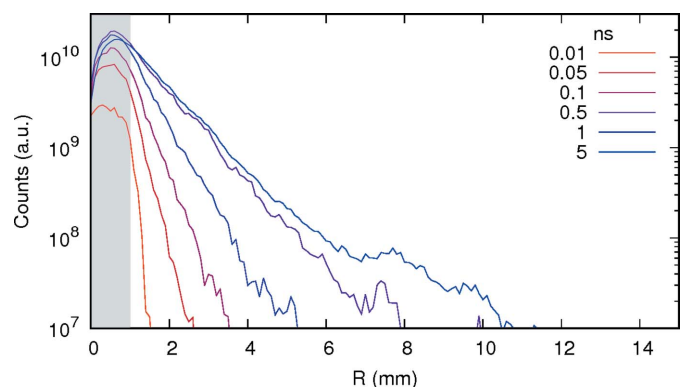


**Figure 8**  
Histogram of the simulated electron population spatial distribution at different MC simulation times after the arrival of an X-ray flash. The grey area represents the area exposed to the X-ray beam. Simulation for 200 mbar Ar,  $2\text{ mm} \times 2\text{ mm}$  beam size, U18 undulator spectrum (see Fig. 1). Bin size: 0.1 mm.

most of the electrons have an energy lower than the ionization energy and no growth of their population occurs afterwards. The resulting output is then used as input to the fluid model to obtain the steady state of the attenuator.

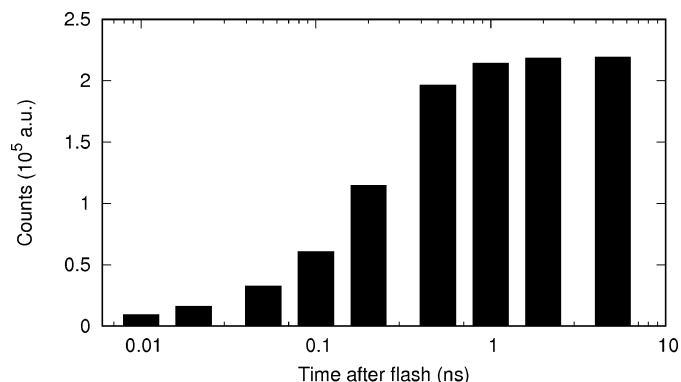


**Figure 9** Total number of electrons in the MC simulation as a function of the time after the arrival of an X-ray flash. Simulation for 200 mbar Ar, 2 mm × 2 mm beam size, U18 undulator spectrum (see Fig. 1).

The time scale in which all the electrons are cooled down below the excitation threshold is of the same order of magnitude, or even longer, than the time between X-ray flashes (2.84 ns). Therefore, there is no significant ‘dark’ period in which the electron population may diffuse and recombine before the next flash arrives. This indicates that, at least for this time structure, we can treat the electron source as continuous in the fluid model, allowing to reach a stationary state without any periodical variations.

#### 4.2. Fluid model results

The stationary solutions of the fluid equations were obtained by running a time-dependent simulation for a long simulated time (100 s), until the obtained radial profiles no longer changed with time. The results are shown in Fig. 10 for charged particle distributions, excited-states distributions, electric potential, electron temperature and gas temperature and density. The absolute particle number density (Fig. 10a)

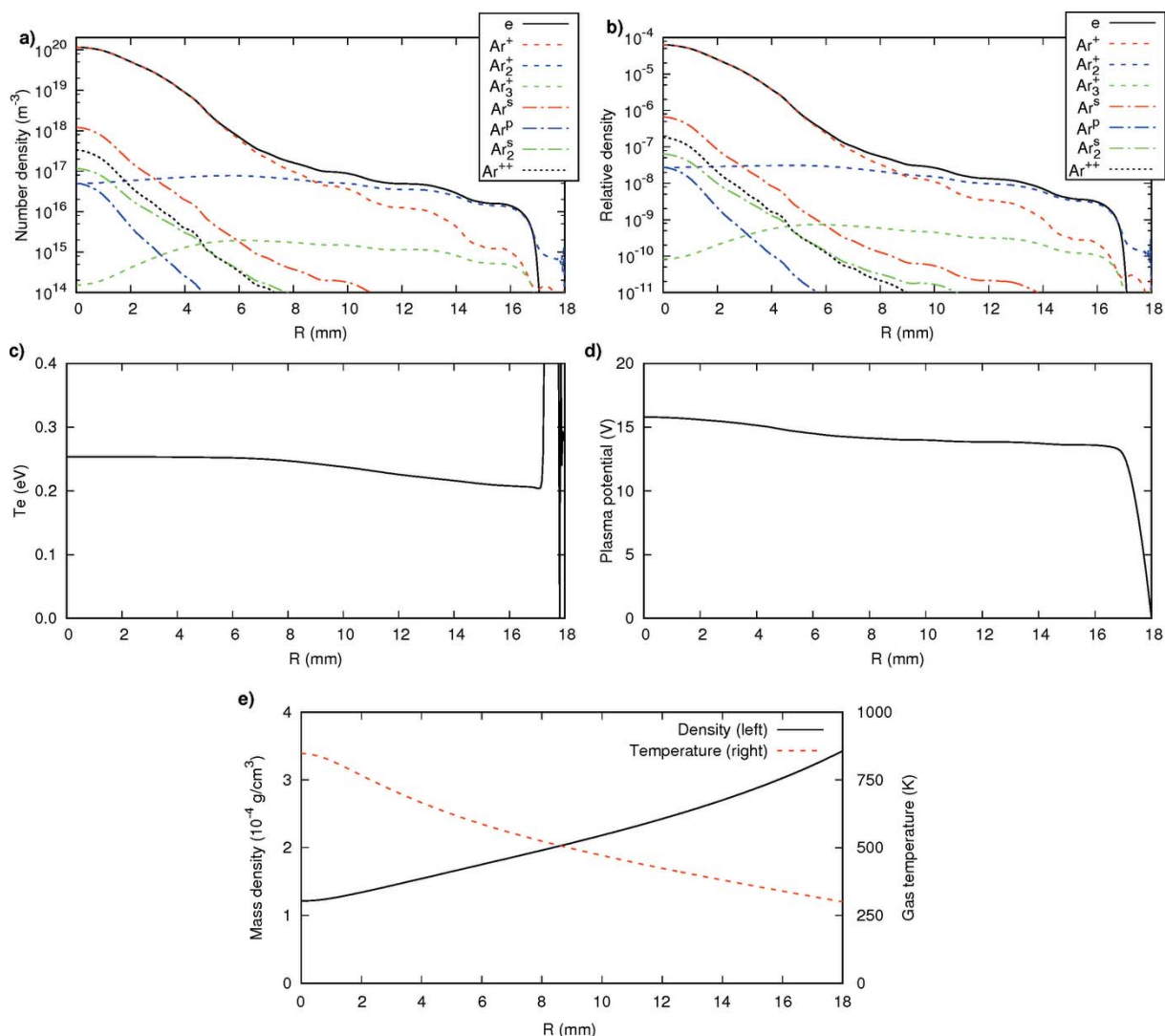


**Figure 10** Outputs of the plasma simulation as a function of the radial position using the global model in 2D (see Figs. 2 and 3). The absolute and relative particle number densities have been plotted separately to account for the change in the total gas density.

and that relative to the total number density (Fig. 10*b*) are shown separately to account for the changes in the total gas density due to the gas temperature gradient. The dominant ion is the monoatomic ion around the axis of the attenuator ( $r = 0$ ), where the ionization degree is the highest, and the diatomic ion closer to the wall ( $r > 10$  mm), where the ionization degree is smaller and the heavy species reactions dominate. The triatomic ion plays only a secondary role, with its density being below 10% of the electron density and only near the attenuator wall. The excited neutral species are only present near the attenuator axis, with virtually no presence outside this central region. The reason for this is that the diffusion during the lifetime of the radiative excited states is so slow that they emit the photons almost at the same location where the excitation occurs, which is mainly in the region where the X-ray is absorbed. The particle densities far from the attenuator axis ( $r > 8$  mm) are heavily affected by the source term, which comes from the MC module, so that the oscillations arising from the small statistics in this region result in oscillations in the source term and the particle density. To avoid this problem, the source terms are strongly smoothed for  $r > 8$  mm; this smoothing may not be necessary for lower-pressure situations where the diffusion of particles increases and recombination decreases.

The plasma potential (Fig. 10*d*) remains at a low value in all of the volume of the attenuator, reaching a peak of  $\sim 16$  V at the centre and  $\sim 14$  V before the sheath near the wall, at 17 mm from the centre. This corresponds to an average electric field of  $1.25 \text{ V cm}^{-1}$ , clearly insufficient to heat the electron population but characteristic for an ambipolar field. For example, the mean free path of the cold electrons is of the order of 10 to 100  $\mu\text{m}$ , so that the energy gain between collisions is of 1.25 to 0.125 meV assuming a trajectory parallel to the electric field. The electron temperature is correspondingly low, with an almost constant value of  $\sim 0.25$  eV everywhere except near the attenuator wall (Fig. 10*c*). These results are in agreement with measurements of the electron temperature of pulsed UV-generated plasma at mbar pressure, where the electron population cools down to room temperature in a few microseconds (Beckers *et al.*, 2016). The oscillations of the electron temperature in the plasma sheath, near the wall, come from the small number of electrons present in this region. The diffusion and mobility of electrons towards the wall is increased in the sheath, and small imbalances between the transport of electrons and electron energy leads to large changes in the average energy per electron and electron temperature.

Finally, the gas temperature and total mass density are shown in Fig. 10(*e*). These are the key values required from the model, since it is the gas mass density that determines the degree of X-ray absorption, plasma source and gas heating. In this case, the temperature at the centre reaches more than 800 K from the initial 300 K near the wall, and the density decreases accordingly to about one-third of its value near the attenuator wall. The gas density gradient is quite smooth, and the variations around the centre of the attenuator are relatively small. Therefore, one can use the value of the gas

**Table 2**

Power balance of the most important energy transfer channels to the wall from the global model (Fig. 2) for 200 mbar argon gas.

Loss mechanism		Power loss ( $\text{W cm}^{-1}$ )	Power loss fraction (%)
X-ray absorption	Absorbed power	1.82	100
	Photoionization	1.78	97.8
	Scattering	0.04	2.2
	Photoelectrons	1.27	69.8
Fluorescent and Auger decay	Auger electrons	0.45	24.7
	X-ray fluorescence	0.04	2.2
	Potential energy (ions)	0.02	1.1
	Input (fast electrons and ions)	1.74	95.6
	Slow electrons	0.27	14.8
Electron slow down (MC)	Single ions	0.85	46.7
	Multiple ions	0.11	6.1
	Excited species	0.48	26.4
	Elastic losses	0.03	1.6
	$\text{Ar}^s$ radiation	1.05	57.7
	$\text{Ar}^p$ radiation	0.23	12.6
Fluid model	$\text{Ar}_2^s$ radiation	0.01	0.05
	Heating: electron collision	0.26	14.3
	Heating: heavy species reactions	0.13	7.1
	Heating: total	0.40	22.0

density at the centre to calculate the X-ray transmission through each particular gas slice.

We can also compare here the validity of the assumption made of taking the X-ray beams as continuous, despite their time structure. The total number of electrons created in one single flash and a slice of 1 cm thickness, at the end of the thermalization calculated by the MC model, was  $6.63 \times 10^8 \text{ cm}^{-1}$ , integrated in the whole 2D domain. The total number of electrons in the steady state calculated by the fluid model is  $4.9 \times 10^{15} \text{ cm}^{-1}$ , again integrated in the 2D domain. Therefore, the electrons on a single pulse are only  $1.35 \times 10^{-7}$  of the steady-state ones. We see that the individual flashes will not impact greatly on the steady state, and it is only by the accumulation of many flashes that the stationary state is reached. This process should be verified when using the same model for different time structures of an X-ray beam.

### 4.3. Power balance

The power balance of all the processes involved is shown in Table 2, including both the initial absorption and Auger decay, the electron thermalization and the output of the fluid model. We can observe that most of the power ( $1.78 \text{ W cm}^{-1}$  out of  $1.82 \text{ W cm}^{-1}$ ) is indeed absorbed as photoionization, and it is taken in turn by fast (photo- and Auger) electrons. The small amount of energy carried by scattered and fluorescent X-rays ( $0.08 \text{ W cm}^{-1}$ ) is assumed to escape the gas and reach the walls of the attenuator. The collisional cascades triggered by the fast electrons results in the transfer of a significant amount of energy from kinetic to potential energy in excited and ionized atoms ( $1.46 \text{ W cm}^{-1}$  out of  $1.74 \text{ W cm}^{-1}$  of the fast electrons); the electrons still carry a significant amount of

kinetic energy ( $0.27 \text{ W cm}^{-1}$ ) but it is no longer the main energy transfer mechanism. This is also observed in the fluid model energy transfer, where the main energy-loss mechanism is the radiative deexcitation from both  $\text{Ar}^s$  and  $\text{Ar}^p$  states ( $1.28 \text{ W cm}^{-1}$ ). Note that the sum of the radiated energy is greater than that of the excited states generated by the fast electrons. The difference comes from the diatomic recombination, which ends up with a neutral excited atom which will also decay emitting further radiation. All this radiation eventually escapes the bulk of the gas without heating it, reaching the walls of the attenuator. Only a fraction of the initial absorbed power actually heats up the gas, both *via* electron elastic collisions and *via* heat released on heavy species reactions.

### 5. Comparison of the 3D model with experimental results

The results obtained in the model can be compared with experimental results on a prototype of an ESRF gas attenuator. Details of the experimental arrangement are given in a separate paper (Martín Ortega *et al.*, 2017). However, we briefly present here the method used. Two quantities were measured that can be compared with the model: the spatial distribution of the excited states of argon and the total power absorbed by the attenuator. The distribution of  $\text{Ar}^p$  states was measured using optical emission spectroscopy (OES), and the distribution of the  $\text{Ar}(1s_5)$  metastable state by tunable laser absorption spectroscopy (TLAS). Both techniques were performed at a single longitudinal position at 120 mm from the entrance of the attenuator, in two separate experimental campaigns. Simultaneously to both OES and TLAS, the absorbed X-ray power was measured using two independent techniques: (i) the calorimetry of the incident and transmitted X-ray beam, and (ii) the X-ray absorption at a selected energy, from which the gas density and therefore the absorption of the complete spectrum can be calculated.

#### 5.1. Excited-states profile

The excited-states radial distribution obtained from the model is compared with those obtained experimentally in Fig. 11. The longitudinal position along the attenuator of the modelled slice has a negligible impact on the excited-species profile and only affects their absolute value. Because the measurements of the  $\text{Ar}^p$  levels only yield relative values, all the profiles have been normalized to its maximum value. The absolute values of  $\text{Ar}^s$  obtained experimentally could be compared directly with those of the model; however, they are highly dependent on the effective deexcitation rate, which is set manually to an approximate value in the model. Differences as large as three orders of magnitude (from  $10^{-8}$  to  $10^{-6} \text{ s}^{-1}$ ) on this deexcitation rate do not affect the excited-states profile or any other output of the model, showing that the profile depends only on the source term obtained from the MC model. Hence, the profile and the absolute value of the excited states are actually independent.

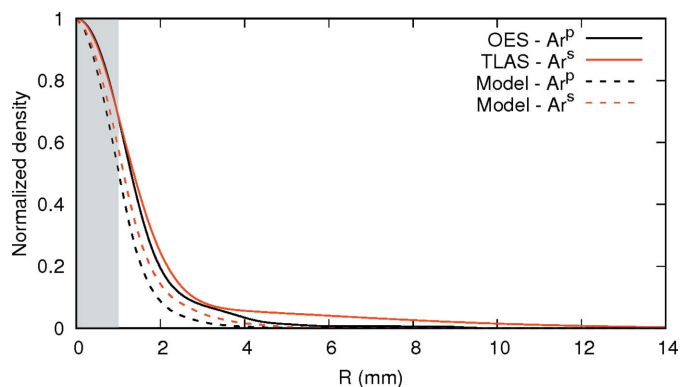


**Figure 11** OES profile, TLAS profile and simulated excited-states profiles for 200 mbar argon, an X-ray source from a U18 undulator at 6 mm and a beam size of  $2 \text{ mm} \times 2 \text{ mm}$ . The profiles have been normalized to their respective maximum values. The grey area represents the region exposed to the X-ray beam.

Both experimentally measured excited-state densities show a very similar profile, which has the same characteristics as that obtained in the model: a central peak around the X-ray beam path which decays quickly outside this region to a low value, which extends down to the attenuator wall. The profile of  $\text{Ar}^s$  is slightly broader than that of  $\text{Ar}^p$  in both experiment and model. This general trend is also reproduced in the model, although the decay is much faster and the density in the wings much lower than in the experiment. This characteristic is common to all the cases studied, which indicates that some mechanisms exciting the neutral atoms of the gas have not been taken into account in the model. For instance, a possible missing mechanism is the interaction of fluorescent and scattered X-rays within the gas; however, they carry a very small fraction of the power and their interaction probability before reaching the walls is small, so that it is unlikely that this is the cause. A more likely reason is a longer range of the fast electrons, so that the region in which they excite and ionize atoms before thermalizing is larger than simulated. A different EEDF could increase the diffusion of cold electrons, increasing its density further away from the attenuator axis and creating more argon excited states there. Finally, the resonant photon transport is simplified by assuming a longer lifetime; the actual transport may affect the spatial profile of the  $\text{Ar}^s$  states in a manner not taken into account in the model.

#### 5.2. Total power absorption (3D model)

To be able to compare directly the model with experimental results, we need to go from the 2D model to the 3D attenuator. In principle, one could do this by simulating adjacent 2D slices, the X-ray input of each slice being the output of the previous one. However, this would require a large number of simulations. Instead, one could consider that the changes in gas density and temperature will be gradual along the beam axis, and characterized by a much smaller gradient compared with the radial profiles. Therefore, it would be possible to simulate only a limited set of 2D slices and interpolate between them.

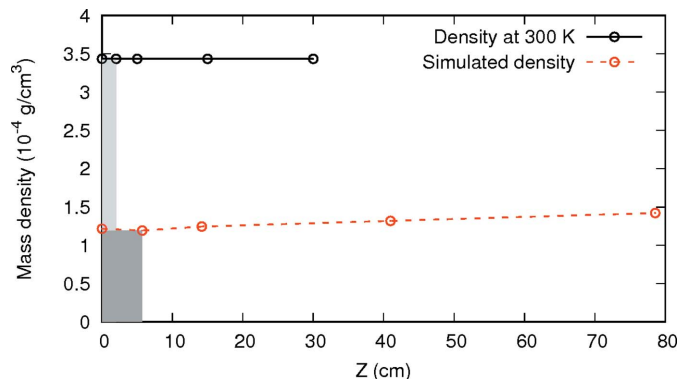


**Figure 12** Position of the simulated 1 cm slices assuming constant, room-temperature mass density (continuous line) and interpolating the mass density obtained with the simulation (dashed line). The grey areas have equal size, therefore providing the same X-ray absorption before the second simulated point. The simulation parameters were 200 mbar of argon gas, 18 mm of attenuator radius and X-ray spectrum corresponding to a U18 undulator with 2 mm × 2 mm beam size.

The problem is that to simulate a slice of gas attenuator at a distance  $z$  of the entrance we have to know the mass of gas in front of this slice,  $\int \rho(z) dz$ , to calculate the incident X-ray beam  $I_{in,z}$  to the simulated slice,

$$I_{in,z}(E) = I_0(E) \exp \left[ -\sigma(E) \int_0^z \rho(z) dz \right]. \quad (19)$$

At this stage, that mass is still unknown because we need to interpolate the density between the entrance and the simulated slice. But it is not the density that determines the absorption and therefore the incident beam but rather the total amount of mass. Therefore, we could have the same incident beam with a different gas density in front of the simulated slice by just changing the position of the slice. In particular, we could make the simulation assuming a constant density  $\rho_0$  and a position  $z_0$ ; these values are just taken as auxiliaries. Once the actual density  $\rho(z)$  of the simulation is obtained, we can recalculate the corresponding  $z$  position,

$$\int_0^z \rho(z) dz = \rho_0 z_0. \quad (20)$$

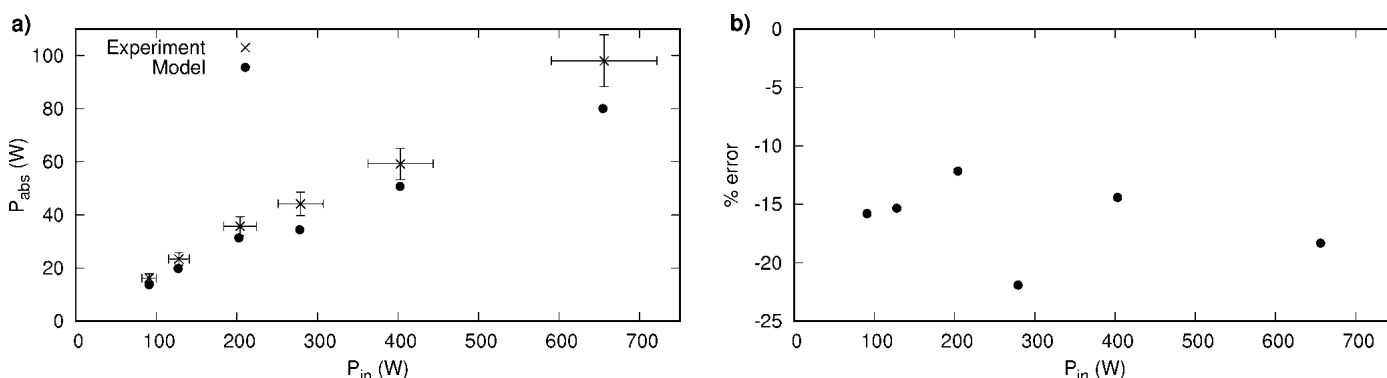


**Figure 13** Power absorption measured experimentally and predicted by the model (a) and relative error of the model prediction (b) versus incident X-ray power, for 200 mbar argon gas. The source was a U18 undulator using different gaps and beam sizes.

This is represented graphically in Fig. 12, where the red line represents the initial positions assuming 200 mbar of pressure and 300 K and the blue line the recalculated positions with the density obtained from the simulation. The number and position of the initial slices should be specified in each case to take into account the larger gradients that may appear in the frontal part of the attenuator; for instance, larger pressure means larger absorption and likely larger gradients than in the case of lower pressure, where the absorption and the gradients might be smaller.

The proposed model was applied to the experimental conditions described in a separate paper (Martín Ortega *et al.*, 2017), in particular to the cases with 200 mbar of initial pressure. The attenuator was considered as a cylinder of length 50.8 cm and radius 18 mm; the protruding ports and flanges carrying the gas feeding and pumping systems, the optical measurement ports and the details of the ends of the gas chamber were not considered in the model. The results of the total absorbed power and of the error relative to the measured absorbed power are shown in Fig. 13. The error bars in the experimental power absorption correspond to around 10% of its total value. The simulated power absorption was found to be lower than the experimentally measured one, with a difference between 10 and 22% of the absorbed power. A lower power absorption than measured means an average gas density also lower than in reality, and therefore a higher gas temperature. The outcome is that the gas is heated more efficiently in the simulation than in reality, or that the cooling is less efficient.

There are several reasons for which the gas temperature obtained in the model may be higher (and the power absorption lower) than the measured one. In the first place, the flanges and especially the water-cooled attenuator windows have not been modelled; they may absorb part of the heating and reduce the gas temperature in the surrounding area. Secondly, the EEDF may be non-Maxwellian. This would affect both the electron–ion recombination rate and the electron–neutral collision frequency, which accounts for an important fraction of the heating power; a change in these values could lead to changes in the gas temperature. An additional effect of a non-Maxwellian EEDF is a change in the electron transport, which in turn may extend the size of the

heated region, again changing the gas temperature. Finally, dynamical turbulence or instabilities in the gas and plasma would enhance the heat transfer towards the walls, reducing the gas temperature and increasing the density and power absorption. This work has focused on the stationary state and properties of the plasma; a dynamical measurement of its properties could provide an insight into these additional cooling mechanisms.

## 6. Conclusions

A hybrid model of the gas attenuator combining the analytical description of the high-energy synchrotron radiation absorption, the MC model of the fast photoelectrons and the fluid model of the diffusive plasma has been developed. The high-energy and MC models simulate the X-ray absorption, ion deexcitation and fast electron thermalization, giving as output the slowed-down electron population together with the number of ions and excited species created. According to this model, the fast electrons created after the X-ray absorption thermalize within a few nanoseconds in a region only slightly larger (1–2 mm larger radius) than the X-ray beam cross section. This electron population is taken as input by the fluid model, which solved the diffusion and recombination of ions and electrons, the decay of excited species and the heating of the gas. The resulting plasma was confined around the X-ray beam, recombining in the bulk of the gas with the diatomic ion of argon,  $\text{Ar}_2^+$ . The plasma potential was found to be low ( $\sim 15$  V) due to the absence of applied electric fields. The electron temperature was also found to be rather low, around 0.2 to 0.3 eV, in agreement with other studies in plasmas created by EUV laser pulses. The gas temperature and density also exhibited large radial gradients, with the temperature being as high as 850 K for 182 W of absorbed power and the density around one-third of that next to the cooled walls.

This hybrid model is able to reproduce the increase of the absorbed power with the input power, with an error contained between 10 and 20% of lower absorption than in the experiment for the studied cases. Also, it is able to reproduce the confinement of the excited species due to the high pressure, with the excited-species profile being somewhat narrower in the model than in the experiment. Overall, the model has been able to reproduce correctly the type of plasma present in the gas attenuator, with the small differences coming possibly from the necessary simplifications made regarding the EEDF or the geometry of the system. This work has focused on the stationary state and properties of the plasma; a dynamical measurement of its properties could provide an insight into additional cooling mechanisms.

The modelling approach developed in this paper can be applied directly to existing gas attenuators to predict the absorption for current and future working conditions, enabling a more efficient operation by reducing the commissioning time determining the power absorption and transmission of the attenuator. It can also be applied to the design of future attenuators, by simulating different geometries and helping to determine which one will be better adapted to the

given physical and technological constrains. This includes not only attenuators for synchrotron beamlines but also attenuators for X-ray free-electron lasers, in which the time-averaged emitted power has a similar value. In this case, the model should be modified to take into account the different time structure of these sources. In particular, equations (11)–(16) of the fluid model should be modified to include the time derivatives of the variables involved, and the source of plasma species obtained from the MC model should not be treated as stationary but should reproduce the time structure of the incident X-ray beam. The main consequence is that the gas might cool down significantly in the inter-pulse interval, increasing the gas density with respect to that of the stationary state and therefore the X-ray absorption. However, as the essential physical processes described in this model would remain the same, the present model is a solid basis for further developments.

## Acknowledgements

The authors would like to acknowledge the contribution of Manuel Sánchez del Río for useful discussions.

## References

- Abdullah, A. H., El-Shemi, A. M. & Ghoneim, A. A. (2003). *Radiat. Phys. Chem.* **68**, 697–705.
- Agostinelli, S., Allison, J., Amako, K., Apostolakis, J., Araujo, H., Arce, P., Asai, M., Axen, D., Banerjee, S., Barrand, G., Behner, F., Bellagamba, L., Boudreau, J., Broglia, L., Brunengo, A., Burkhardt, H., Chauvie, S., Chuma, J., Chytracsek, R., Cooperman, G., Cosmo, G., Degtyarenko, P., Dell'Acqua, A., Depaola, G., Dietrich, D., Enami, R., Feliciello, A., Ferguson, C., Fesefeldt, H., Folger, G., Foppiano, F., Forti, A., Garelli, S., Giani, S., Giannitrapani, R., Gibin, D., Gómez Cadenas, J. J., González, I., Gracia Abril, G., Greeniaus, G., Greiner, W., Grichine, V., Grossheim, A., Guatelli, S., Gumplinger, P., Hamatsu, R., Hashimoto, K., Hasui, H., Heikkinen, A., Howard, A., Ivanchenko, V., Johnson, A., Jones, F. W., Kallenbach, J., Kanaya, N., Kawabata, M., Kawabata, Y., Kawaguti, M., Kelner, S., Kent, P., Kimura, A., Kodama, T., Kokoulin, R., Kossov, M., Kurashige, H., Lamanna, E., Lampén, T., Lara, V., Lefebvre, V., Lei, F., Liendl, M., Lockman, W., Longo, F., Magni, S., Maire, M., Medernach, E., Minamimoto, K., Mora de Freitas, P., Morita, Y., Murakami, K., Nagamatu, M., Nartallo, R., Nieminen, P., Nishimura, T., Ohtsubo, K., Okamura, M., O'Neale, S., Oohata, Y., Paech, K., Perl, J., Pfeiffer, A., Pia, M. G., Ranjard, F., Rybin, A., Sadilov, S., Di Salvo, E., Santin, G., Sasaki, T., Savvas, N., Sawada, Y., Scherer, S., Sei, S., Sirotenko, V., Smith, D., Starkov, N., Stoecker, H., Sulkimo, J., Takahata, M., Tanaka, S., Tcherniaev, E., Safai Tehrani, E., Tropeano, M., Truscott, P., Uno, H., Urban, L., Urban, P., Verderi, M., Walkden, A., Wander, W., Weber, H., Wellisch, J. P., Wenaus, T., Williams, D. C., Wright, D., Yamada, T., Yoshida, H. & Zschiesche, D. (2003). *Nucl. Instrum. Methods Phys. Res. A*, **506**, 250–303.
- Aleksandrov, N. L. (2005). *Plasma Phys. Rep.* **31**, 425.
- Allison, J., Amako, K., Apostolakis, J., Araujo, H., Arce Dubois, P., Asai, M., Barrand, G., Capra, R., Chauvie, S., Chytracsek, R., Cirrone, G., Cooperman, G., Cosmo, G., Cuttano, G., Daquino, G., Donszelmann, M., Dressel, M., Folger, G., Foppiano, F., Generowicz, J., Grichine, V., Guatelli, S., Gumplinger, P., Heikkinen, A., Hrivnacova, I., Howard, A., Incerti, S., Ivanchenko, V., Johnson, T., Jones, F., Koi, T., Kokoulin, R., Kossov, M., Kurashige, H., Lara, V., Larsson, S., Lei, F., Link, O., Longo, F., Maire, M., Mantero, A., Mascialino, B., McLaren, I., Mendez Lorenzo, P., Minamimoto, K.,

- Murakami, K., Nieminen, P., Pandola, L., Parlati, S., Peralta, L., Perl, J., Pfeiffer, A., Pia, M., Ribon, A., Rodrigues, P., Russo, G., Sadilov, S., Santin, G., Sasaki, T., Smith, D., Starkov, N., Tanaka, S., Tcherniaev, E., Tome, B., Trindade, A., Truscott, P., Urban, L., Verderi, M., Walkden, A., Wellisch, J., Williams, D., Wright, D. & Yoshida, H. (2006). *IEEE Trans. Nucl. Sci.* **53**, 270–278.
- Baruchel, J., Hodeau, J. L., Lehmann, M. S., Regnard, J. R. & Schlenker, C. (1993). *Neutron and Synchrotron Radiation for Condensed Matter Studies*, Volume I, *Theory, Instruments and Methods*. Berlin and Les Ulis: Springer and Les Editions de Physique.
- Beckers, J., van der Horst, R. M., Osorio, E. A., Kroesen, G. M. W. & Banine, V. Y. (2016). *Plasma Sources Sci. Technol.* **25**, 035010.
- Biagi, S. (2015). *Biagi-v8.9 database*, <http://www.lxcat.net> (retrieved on 1 July 2015).
- Biasci, J.-C., Plan, B. & Zhang, L. (2002). *J. Synchrotron Rad.* **9**, 44–46.
- Biberman, L. M., Vorob'ev, V. S. & Iakubov, I. T. (1987). *Kinetics of Nonequilibrium Low-Temperature Plasma*. New York: Plenum.
- Bich, E., Millat, J. & Vogel, E. (1990). *J. Phys. Chem. Ref. Data*, **19**, 1289–1305.
- Bogaerts, A. & Gijbels, R. (1999). *J. Appl. Phys.* **86**, 4124–4133.
- Bordage, M. C., Biagi, S. F., Alves, L. L., Bartschat, K., Chowdhury, S., Pitchford, L. C., Hagelaar, G. J. M., Morgan, W. L., Puech, V. & Zatsarinny, O. (2013). *J. Phys. D*, **46**, 334003.
- Brennan, M. J. (1991). *IEEE Trans. Plasma Sci.* **19**, 256–261.
- Carbone, E. A. D., Hübner, S., van der Mullen, J. J., Kroesen, G. M. W. & Sadeghi, N. (2013). *J. Phys. D*, **46**, 415202.
- Carlson, T. A., Hunt, W. E. & Krause, M. O. (1966). *Phys. Rev.* **151**, 41.
- Chang, R. S. F. & Setser, D. W. (1978). *J. Chem. Phys.* **69**, 3885–3897.
- Chen, C. J. (1969). *Phys. Rev.* **177**, 245–254.
- Chubar, O. & Elleaume, P. (1998). *Proceedings of the Sixth European Particle Accelerator Conference (EPAC'98)*, pp. 1177–1179.
- Chumakov, A., Rüffer, R., Leupold, O., Celse, J.-P., Martel, K., Rossat, M. & Lee, W.-K. (2004). *J. Synchrotron Rad.* **11**, 132–141.
- COMSOL (2017a). *COMSOL Multiphysics Reference Manual*, Version 5.2. Comsol, Inc., Burlington, MA, USA.
- COMSOL (2017b). *Plasma Module User's Guide*, Version 5.2. Comsol, Inc., Burlington, MA, USA.
- Cullen, D. E., Hubbell, J. H. & Kissel, L. (1997). *The Evaluated Photon Data Library*. Technical Report. Lawrence Livermore National Laboratory, Livermore, CA, USA.
- Elson, E. & Rokni, M. (1996). *J. Phys. D*, **29**, 716–725.
- Feng, Y., Krzywinski, J., Schafer, D. W., Ortiz, E., Rowen, M. & Raubenheimer, T. O. (2016). *J. Synchrotron Rad.* **23**, 21–28.
- Gavrila, M. (1959). *Phys. Rev.* **113**, 514–526.
- Hagelaar, G. J. M. & Pitchford, L. C. (2005). *Plasma Sources Sci. Technol.* **14**, 722–733.
- Hernández, C. F. (2010). Master's thesis. ETSII Madrid, Grenoble INP, France.
- Howorka, F. (1977). *J. Chem. Phys.* **67**, 2919.
- Hussein, M. A., Emmert, G. A., Hershkowitz, N. & Claude Woods, R. (1992). *J. Appl. Phys.* **72**, 1720–1728.
- Kobayashi, A., Fujiki, G., Okaji, A. & Masuoka, T. (2002). *J. Phys. B*, **35**, 2087–2103.
- Martín Ortega, Á., Lacoste, A., Béchu, S., Bès, A. & Sadeghi, N. (2017). *J. Synchrotron Rad.* **24**, 1195–1208.
- Mehr, F. J. & Biondi, M. A. (1968). *Phys. Rev.* **176**, 322–326.
- Mills, J. & Hieftje, G. (1984). *At. Spectrosc.* **39**, 859–866.
- Neeser, S., Kunz, T. & Langhoff, H. (1997). *J. Phys. D*, **30**, 1489–1498.
- Oka, T., Kogoma, M., Imamura, M., Arai, S. & Watanabe, T. (1979). *J. Chem. Phys.* **70**, 3384–3389.
- Opal, C. B., Peterson, W. K. & Beaty, E. C. (1971). *J. Chem. Phys.* **55**, 4100–4106.
- Perkins, S. T., Cullen, D. E., Chen, M. H., Hubbell, J. H., Rathkopf, J. & Scofield, J. (1991b). *Tables and Graphs of Atomic Subshell and Relaxation Data Derived from the LLNL Evaluated Atomic Data Library (EADL), Z = 1–100*. Technical Report. Lawrence Livermore National Laboratory, Livermore, CA, USA.
- Perkins, S., Cullen, D. & Seltzer, S. (1991a). *Tables and Graphs of Electron-Interaction Cross Sections from 10 eV to 100 GeV Derived from the LLNL Evaluated Electron Data Library (EEDL), Z = 1–100*. Technical Report. Lawrence Livermore National Laboratory, Livermore, CA, USA.
- Petrov, G. M. & Ferreira, C. M. (2013). *arXiv:1308.2593*.
- Requardt, H., Renier, M., Brochard, T., Bräuer-Krisch, E., Bravin, A. & Suortti, P. (2013). *J. Phys. Conf. Ser.* **425**, 022002.
- Ryutov, D. D., Bionta, R. M., Kishiyama, K. I., McMahon, D., Roeben, M. D., Shen, S. & Stefan, P. M. (2009). *The Physics of the Gas Attenuator for the Linac Coherent Light Source*. Technical Report LCLS-TN-09-5. LCLS, SLAC National Accelerator Laboratory, CA, USA.
- Saloman, E., Hubbell, J. & Scofield, J. (1988). *At. Data Nucl. Data Tables*, **38**, 1–196.
- Salvat, F. & Fern, M. (2015). *PENELOPE – A Code System for Monte Carlo Simulation of Electron and Photon Transport*. Organisation for Economic Co-operation and Development.
- Sempau, J., Acosta, E., Baro, J., Fernández-Varea, J. M. & Salvat, F. (1997). *Nucl. Instrum. Methods Phys. Res. B*, **132**, 377–390.
- Skullerud, H. R. (1968). *J. Phys. D*, **1**, 1567–1568.
- Takizuka, T. & Abe, H. (1977). *J. Comput. Phys.* **25**, 205–219.
- Thompson, A. C. & Vaughan, D. (2001). *X-ray Data Booklet*, 2nd ed. Lawrence Berkeley National Laboratory, University of California, USA.
- Turner, D. L. & Conway, D. C. (1979). *J. Chem. Phys.* **71**, 1899–1901.
- Vahedi, V. & Surendra, M. (1995). *Comput. Phys. Commun.* **87**, 179–198.
- Verboncoeur, J. P. (2005). *Plasma Phys. Contrib. Fusion*, **47**, A231–A260.
- Vriens, L. & Smeets, A. H. M. (1980). *Phys. Rev. A*, **22**, 940–951.
- Wiese, W. & Martin, G. (1980). *Wavelengths and Transition Probabilities for Atoms and Atomic Ions*, Part 2, *Transition Probabilities*. NSRDS-NBS 68. Center for Radiation Research, National Measurement Laboratory, National Bureau of Standards, Washington, DC, USA.
- Zhang, L., Sánchez del Río, M., Monaco, G., Detlefs, C., Roth, T., Chumakov, A. I. & Glatzel, P. (2013). *J. Synchrotron Rad.* **20**, 567–580.